

**This manuscript has been accepted for publication in Nature Photonics:**

Harter, T., Muehlbrandt, S., Ummethala, S., Schmid, A., Nellen, S., Hahn, L., Freude, W., & Koos, C. Silicon-plasmonic integrated circuits for terahertz signal generation and coherent detection. *Nature Photonics* **12**, 625–633. (2018)  
<https://doi.org/10.1038/s41566-018-0237-x>

# Silicon-plasmonic integrated circuits for terahertz signal generation and coherent detection

T. Harter<sup>1,2\*</sup>, S. Muehlbrandt<sup>1,2</sup>, S. Ummethala<sup>1,2</sup>, A. Schmid<sup>1</sup>, S. Nellen<sup>3</sup>, L. Hahn<sup>2</sup>, W. Freude<sup>1</sup>, C. Koos<sup>1,2\*\*</sup>

<sup>1</sup>*Institute of Photonics and Quantum Electronics (IPQ), Karlsruhe Institute of Technology (KIT), 76131 Karlsruhe, Germany*

<sup>2</sup>*Institute of Microstructure Technology (IMT), Karlsruhe Institute of Technology (KIT), 76344 Eggenstein-Leopoldshafen, Germany*

<sup>3</sup>*Fraunhofer Institute for Telecommunications, Heinrich Hertz Institute (HHI), 10587 Berlin, Germany*

\*[tobias.harter@kit.edu](mailto:tobias.harter@kit.edu), \*\*[christian.koos@kit.edu](mailto:christian.koos@kit.edu)

**Optoelectronic signal processing offers great potential for generation and detection of ultra-broadband waveforms in the THz range, so-called T-waves. However, fabrication of the underlying devices still relies on complex processes using dedicated III-V semiconductor substrates. This severely limits the application potential of current T-wave transmitters and receivers, in particular when it comes to highly integrated systems that combine photonic signal processing with optoelectronic conversion to THz frequencies. In this paper, we demonstrate that these limitations can be overcome by plasmonic internal-photo-emission detectors (PIPED). PIPED can be realized on the silicon photonic platform and allow to leverage the enormous opportunities of the associated device portfolio. In our experiments, we demonstrate both T-wave signal generation and coherent detection at frequencies of up to 1 THz. To proof the viability of our concept, we monolithically integrate PIPED transmitters and PIPED receivers on a common silicon photonic chip and use them for measuring the complex transfer impedance of an integrated T-wave device.**

Terahertz signals (T-waves) offer promising perspectives for a wide variety of applications, comprising high-speed communications<sup>1–3</sup>, microwave photonics<sup>4</sup>, spectroscopy<sup>5,6</sup>, life sciences<sup>7,8</sup>, as well as industrial metrology<sup>9,10</sup>. Optoelectronic signal processing techniques are particularly attractive both for T-wave generation<sup>11,12</sup> and detection<sup>13,14</sup>, especially when broadband tunability of the THz frequency is required. On a conceptual level, optoelectronic generation of continuous-wave (CW) THz signals relies on mixing of two optical signals oscillating at frequencies  $f_a$  and  $f_b$  in a high-speed photodetector, for which the photocurrent depends on the incident optical power<sup>11</sup>. The photocurrent oscillates with a difference frequency  $f_{\text{THz}} = |f_a - f_b|$  in the terahertz region, which can be relatively easily adjusted over the full bandwidth of the photodetector by frequency-tuning of one of the two lasers. In many practical applications, the optical signal oscillating at  $f_a$  carries an amplitude or phase modulation, whereas the optical signal at  $f_b$  is simply a CW carrier. In this case, the phase and amplitude modulation of the optical carrier is directly transferred to the T-wave carrier. This concept shows great potential for high-speed wireless communications at THz carrier frequencies and has been at the heart of a series of transmission experiments, in which record-high data rates of 100 Gbit/s and above have been reached<sup>2,15,16</sup>. Similarly, optoelectronic techniques can be used for detection of T-wave signals. In this case, the T-wave signal

is applied to a high-speed photoconductor and the optical power oscillation at the difference frequency  $f_{\text{THz}} = |f_a - f_b|$  is used as a local oscillator for coherent down-conversion to the baseband<sup>13,14</sup>. This technique was initially developed for frequency-domain THz spectroscopy systems offering a widely tunable frequency range and a high signal-to-noise ratio<sup>13,17,18</sup>, and has recently been transferred to THz communications<sup>19</sup>.

For exploiting the tremendous application potential of optoelectronic T-wave processing, monolithic co-integration of photonic devices and T-wave transmitters and receivers are of vital importance. From the technology side, however, optoelectronic T-wave transmitters and receivers are still rather complex, relying on high-speed photodiodes<sup>20–22</sup> or photoconductors<sup>13,23,24</sup> that require dedicated III-V semiconductor substrates that are obtained, e. g., through low-temperature growth of InGaAs/InAlAs multilayer structures<sup>13</sup> and that are not amenable to large-scale photonic integration. This does not only hamper the co-integration of T-wave transmitter and receiver circuitry on a common chip, but also hinders the exploitation of highly developed photonic integration platforms for building advanced optoelectronic T-wave systems that combine photonic signal processing with optoelectronic frequency conversion on a common chip.

In this paper, we demonstrate an approach that allows to integrate T-wave transmitters and receivers directly on the silicon

photonic platform, thereby exploiting the outstanding technical maturity, scalability and the comprehensive device portfolio<sup>25–27</sup> of this material system. The approach exploits internal photoemission at metal-semiconductor interfaces of plasmonic structures<sup>28,29</sup> that can be directly integrated into widely used silicon-on-insulator (SOI) waveguides. Our experiments show that these plasmonic internal-photoemission detectors (PIPED) are not only suited for photomixing in the T-wave transmitter, but also lend themselves to highly sensitive optoelectronic reception. In a proof-of-concept experiment, we monolithically co-integrate a PIPED transmitter and a PIPED receiver on a common silicon photonic chip and use them for measuring the complex transfer function of an integrated T-wave transmission line. In this context, we also develop and experimentally verify a mathematical model of optoelectronic T-wave conversion that allows to quantitatively describe T-wave generation and detection over a wide range of frequencies.

### Silicon-plasmonic T-wave systems

The vision of an integrated silicon-plasmonic T-wave system is illustrated in Fig. 1 using a wireless high-speed transceiver as an exemplary application case. The system combines T-wave transmitter, T-wave receiver and a variety of other silicon photonic devices<sup>25,26</sup> such as phase shifters<sup>31–33</sup> or high-performance modulators<sup>34–37</sup> on a common substrate. Continuous-wave (CW) lasers are coupled to the chip using photonic wire bonds<sup>30</sup>, and electrical circuits such as field-programmable gate arrays (FPGA), digital-to-analogue and analogue-to-digital converters (DAC and ADC) are used to drive the modulators and to further process the received signals. T-wave generation is accomplished by photomixing of modulated optical signals with an optical CW tone in high-speed plasmonic internal-photoemission detectors (PIPED<sup>28</sup>). The antenna-coupled PIPED act as optical-to-T-wave (O/T) converters. Large-scale monolithic integration of advanced silicon photonic devices with O/T converters opens rich opportunities for advanced T-wave signal processing. For integrated T-wave systems, generation and detection of CW signals offers various advantages over pulsed operation, see Methods for details. In the illustration, the transmitter comprises a T-wave antenna array, fed by an array of O/T converters that are driven by a series of optical signals. The phases of the optical signals and hence those of the T-wave signals can be precisely defined by an electrically driven optical phase shifter network<sup>31,32</sup>, thereby enabling broadband beam steering and shaping. Optionally, integrated T-wave amplifiers can be used to boost the T-wave signals<sup>38</sup>. At the receiver, optoelectronic down-conversion (T/E-conversion) is used for coherent detection of the T-wave signal, using the power beat of two optical waves as a local oscillator. For O/T and T/E conversion, the concept relies on PIPED that are coupled to dipole antennae, see Inset 1 of Fig. 1. The PIPED are fed through silicon photonic

waveguides and biased via dedicated low-pass structures that are directly connected to the arms of the dipole antennae. A more detailed view of a PIPED is shown in Inset 2. The device consists of a narrow silicon nanowire waveguide that is combined with overlays of gold (Au) and titanium (Ti) to form an ultra-small plasmonic structure with two metal-semiconductor interfaces. Note that the PIPED concept does not rely on the use of gold as a plasmonic material – this was chosen only for ease of fabrication in the current experiment. When combined with large-scale silicon photonic circuits, gold-free designs may be used that allow the processing in a state-of-the-art CMOS line<sup>39</sup>.

### Plasmonic internal-photoemission detectors (PIPED) for optoelectronic T-wave processing

The PIPED concept is illustrated and explained in Fig. 2. Figure 2a shows a schematic cross section of the device. The Si nanowire waveguide core is contacted by an Au layer on the left and by a Ti layer on the right – details of the fabrication can be found in ref. 28. To drive the device, light at infrared telecommunication wavelengths ( $\lambda \approx 1.54 \mu\text{m}$ ) is coupled to the Si waveguide core, leading to an excitation of surface plasmon polaritons (SPP) both at the Au-Si and at the Si-Ti interfaces – the associated energy levels are sketched in Fig. 2b for a forward bias voltage  $U > 0$ , which is counted positive from the Au to the Ti electrode. Free-carrier absorption generates hot electrons in the titanium with carrier energies above the Fermi level  $W_{\text{F,Ti}}$ . An equivalent effect occurs for holes at the Au-Si-interface – the relative magnitude of the two contributions is currently under investigation. The hot electrons and holes have an increased probability to cross the  $d = 100 \text{ nm}$  wide Si barrier, leading to a photocurrent  $I$  from the Au to the Ti side. The photocurrent  $I$  depends linearly on the optical power  $P$  with a sensitivity (or responsivity)  $S = I / P$ . Note that, in contrast to conventional photodiodes, the measured sensitivity  $S(U)$  of the PIPED depends strongly on the applied voltage  $U$  as shown in Fig. 2c. This voltage dependence is a key aspect for efficient optoelectronic T/E conversion as it allows mixing of an oscillating optical input power with a time-dependent voltage applied to the PIPED contacts. For a forward bias  $U > 0$ , the band edges tilt inside the Si core, Fig. 2b, which reduces the effective width of the potential barrier such that the sensitivity  $S$  increases with  $U$ . For a reverse bias  $U < 0$ , the carrier emission probability is small, and hence the photocurrent remains small. The strong absorption of the SPP allows junction lengths  $\ell$  of less than  $1 \mu\text{m}$  and device capacitances smaller than  $C = 1 \text{ fF}$  (ref. 28). With a load resistance of  $R = 50 \Omega$ , this would lead to an  $RC$  limiting frequency of  $3 \text{ THz}$ . In the current device designs, this limitation is not relevant since the speed is limited by the transit times, for which we estimate  $1 \text{ ps}$  for electrons and  $1.5 \text{ ps}$  for holes. This estimation is based on a voltage drop of  $U = 0.5 \text{ V}$  at the  $100 \text{ nm}$  wide barrier, leading to drift velocities of  $10^7 \text{ cm s}^{-1}$  for

electrons and  $6.5 \cdot 10^5 \text{ cm s}^{-1}$  for holes<sup>40</sup>, close to respective saturation velocity. This limits the bandwidth to approximately 0.44 THz assuming dominating electron transport and to 0.29 THz in case hole transport dominates<sup>41</sup>. The fast device response makes the PIPED an excellent candidate for T-wave generation and reception at frequencies up to 1 THz and above. It is worth noting that the sensitivity of the PIPED can be increased beyond the values depicted in Fig. 2c by applying larger bias voltages. We have previously demonstrated sensitivities of up to 0.12 A/W (ref. 28) – the highest value so far demonstrated for photodetectors based on internal photoemission. This sensitivity still is below the (0.2...0.3) A/W typically achieved for untravelling carrier photodiodes (UTC-PD) designed to operate at frequencies around 0.3 THz (refs. 21,42,43), and we expect that further improvements are possible by optimizing the materials and geometries of the PIPED. Note that the sensitivity of the photodetector is not of utmost importance for generation and detection of T-wave signals, since a smaller sensitivity can be compensated by applying a higher optical power.

For O/T-conversion, the transmitter (Tx) essentially acts as a mixer multiplying two time-dependent optical signals  $E_{\text{Tx},a}(t)$  and  $E_{\text{Tx},b}(t)$  to produce a photocurrent  $I_{\text{Tx}}(t)$  that corresponds to the difference-frequency waveform, see upper part of Fig. 2d. In the following, we only give a short mathematical description of photomixing and optoelectronic down-conversion in the PIPED. A rigorous analysis can be found in the Supplementary Section 1. We assume that the optical signal  $E_{\text{Tx},a}(t)$  oscillates at angular frequency  $\omega_{\text{Tx},a}$  and carries an amplitude modulation  $\hat{E}_{\text{Tx},a}(t)$  and/or a phase modulation  $\varphi_{\text{Tx},a}(t)$ , whereas the optical signal  $E_{\text{Tx},b}(t)$  is simply a CW carrier with constant amplitude  $\hat{E}_{\text{Tx},b}$ , frequency  $\omega_{\text{Tx},b}$  and phase  $\varphi_{\text{Tx},b}$ ,

$$\begin{aligned} E_{\text{Tx},a}(t) &= \hat{E}_{\text{Tx},a}(t) \cos(\omega_{\text{Tx},a}t + \varphi_{\text{Tx},a}(t)), \\ E_{\text{Tx},b}(t) &= \hat{E}_{\text{Tx},b} \cos(\omega_{\text{Tx},b}t + \varphi_{\text{Tx},b}). \end{aligned} \quad (1)$$

The optical power  $P_{\text{Tx}}(t)$  then oscillates at the difference frequency  $\omega_{\text{Tx,THz}} = |\omega_{\text{Tx},a} - \omega_{\text{Tx},b}|$ ,

$$P_{\text{Tx},l}(t) = \hat{P}_{\text{Tx},l}(t) \cos(\omega_{\text{Tx,THz}}t + \varphi_{\text{Tx,THz}}(t)), \quad (2)$$

where the amplitude  $\hat{P}_{\text{Tx},l}(t)$  and the phase  $\varphi_{\text{Tx,THz}}(t)$  of the oscillation are directly linked to the normalized amplitude and to the phase of the optical wave,

$$\hat{P}_{\text{Tx},l}(t) = \hat{E}_{\text{Tx},a}(t) \hat{E}_{\text{Tx},b}, \quad \varphi_{\text{Tx,THz}}(t) = \varphi_{\text{Tx},a}(t) - \varphi_{\text{Tx},b}. \quad (3)$$

When detected by the PIPED (sensitivity  $S_{\text{Tx}}$ ) this leads to an oscillating component in the photocurrent  $I_{\text{Tx}}(t)$ , featuring the same frequency and the same phase as the optical power oscillation,

$$I_{\text{Tx},l}(t) = \hat{I}_{\text{Tx},l}(t) \cos(\omega_{\text{Tx,THz}}t + \varphi_{\text{Tx,THz}}(t)), \quad (4)$$

where

$$\hat{I}_{\text{Tx},l}(t) = S_{\text{Tx}} \hat{E}_{\text{Tx},a}(t) \hat{E}_{\text{Tx},b}. \quad (5)$$

Hence, any modulation of the amplitude  $\hat{E}_{\text{Tx},a}(t)$  or the phase  $\varphi_{\text{Tx},a}(t)$  of the optical signal translates directly into an amplitude and phase modulation of the T-wave. The amplitude of the emitted THz field is linearly connected to the sensitivity  $S_{\text{Tx}}$ , and can be increased by applying a larger forward bias to the PIPED. Exploiting this concept, broadband high-quality THz signals can be generated by using widely available optical communication equipment. The THz field is radiated by an antenna or coupled to a transmission line.

Similarly, PIPED can be used for T/E conversion in the T-wave receiver (Rx), see lower part of Fig. 2d. In this case, the device combines two functionalities, namely the generation of a THz local oscillator (LO) from two optical carriers, and the down-conversion of the received T-wave to the baseband. To this end, the PIPED is fed by a superposition of two unmodulated optical tones, oscillating at frequencies  $\omega_{\text{Rx},a}$  and  $\omega_{\text{Rx},b}$ ,

$$\begin{aligned} E_{\text{Rx},a}(t) &= \hat{E}_{\text{Rx},a} \cos(\omega_{\text{Rx},a}t + \varphi_{\text{Rx},a}), \\ E_{\text{Rx},b}(t) &= \hat{E}_{\text{Rx},b} \cos(\omega_{\text{Rx},b}t + \varphi_{\text{Rx},b}). \end{aligned} \quad (6)$$

This leads to an oscillating power at frequency  $\omega_{\text{Rx,THz}} = |\omega_{\text{Rx},a} - \omega_{\text{Rx},b}|$  with a phase  $\varphi_{\text{Rx,THz}}$ ,

$$P_{\text{Rx},l}(t) = \hat{P}_{\text{Rx},l} \cos(\omega_{\text{Rx,THz}}t + \varphi_{\text{Rx,THz}}), \quad (7)$$

with the abbreviations

$$\hat{P}_{\text{Rx},l} = \hat{E}_{\text{Rx},a} \hat{E}_{\text{Rx},b}, \quad \varphi_{\text{Rx,THz}} = \varphi_{\text{Rx},a} - \varphi_{\text{Rx},b}. \quad (8)$$

At the same time, the PIPED is biased with a DC voltage  $U_{\text{Rx},0}$ , which is superimposed by the time-variant THz signal  $U_{\text{Rx},l}(t)$  generated by the THz antenna. The overall time-dependent voltage applied to the PIPED hence reads

$$U_{\text{Rx}}(t) = U_{\text{Rx},0} + U_{\text{Rx},l}(t), \quad (9)$$

where

$$U_{\text{Rx},l}(t) = \hat{U}_{\text{Rx},l}(t) \cos(\omega_{\text{Tx,THz}}t + \varphi_{\text{Tx,THz}}(t) - \varphi_{\text{Tx,Rx}}). \quad (10)$$

In this relation, the phase at the receiver depends on the phase delay  $\varphi_{\text{Tx,Rx}}$  that the T-wave experiences when propagating from the Tx to the Rx. Due to the voltage-dependent PIPED sensitivity, the time-varying voltage  $U_{\text{Rx}}(t)$  leads to a temporal variation of the sensitivity  $S_{\text{Rx}}(U_{\text{Rx}}(t))$ , oscillating at the frequency  $\omega_{\text{Tx,THz}}$  of the incident T-wave. The PIPED photocurrent is given by the product of the time-variant sensitivity with the time-variant optical power  $P_{\text{Rx},l}(t)$ . For the case of homodyne detection,  $\omega_{\text{Rx,THz}} = \omega_{\text{Tx,THz}} = \omega_{\text{THz}}$ , the baseband current at the output of the Rx PIPED is given by

$$\begin{aligned} I_{\text{BB}}(t) &= I_{\text{BB},0} + I_{\text{BB},1}(t) \\ &= I_{\text{BB},0} + \hat{I}_{\text{BB},1}(t) \cos(\varphi_{\text{BB}}(t)), \end{aligned} \quad (11)$$

where the amplitude  $\hat{I}_{\text{BB},1}(t)$  of the time-variant part of the baseband photocurrent and the associated time-variant phase  $\varphi_{\text{BB}}(t)$  are connected to the amplitude and the phase of the time-variant THz signal  $U_{\text{Rx},1}(t)$ ,

$$\begin{aligned} \hat{I}_{\text{BB},1}(t) &= \frac{1}{2} \left. \frac{dS_{\text{Rx}}}{dU_{\text{Rx}}} \right|_{U_{\text{Rx},0}} \hat{P}_{\text{Rx},1} \hat{U}_{\text{Rx},1}(t), \\ \varphi_{\text{BB}}(t) &= \varphi_{\text{Tx,THz}}(t) - \varphi_{\text{Rx,THz}} + \varphi_{\text{TxRx}}. \end{aligned} \quad (12)$$

For sensitive detection, the slope  $dS_{\text{Rx}}/dU_{\text{Rx}}|_{U_{\text{Rx},0}}$  of the sensitivity as a function of voltage has to be maximized, such that small variations of the THz voltage translate into large variations of the baseband photocurrent amplitude. The phase  $\varphi_{\text{BB}}(t)$  may be properly adjusted with the variable time delay  $\tau_{\text{opt}}$ , see Fig. 3a. A more convenient alternative measurement technique is explained in the Methods.

### Demonstration of T-wave generation and detection

For an experimental demonstration of the PIPED performance in O/T and T/E conversion, we first characterize the Tx and the Rx separately. To this end, we fabricate a PIPED that is connected to an on-chip dipole antenna as shown in Inset 1 of Fig. 1. To supply a bias voltage  $U_{\text{Tx},0}$  to the PIPED, we use bias lines equipped with THz chokes that prevent leakage of THz signals from the antenna, see Supplementary Section 3 for details of the antenna design. Note that the dipole antenna is not optimum for transmitting and receiving THz power over a broad frequency range. We still decided to use this antenna concept due to its small footprint, which allows us to densely integrate large number of PIPED on a test chip. The dipole antennae may be replaced by bigger spiral or bow-tie structures in future devices. For measuring the device performance, we use the setup depicted in Fig. 3a, where the Tx and the Rx are driven by the same lasers for homodyne detection. To increase the sensitivity of T-wave detection, we use a modulated bias voltage  $U_{\text{Tx},0}$  that leads to a modulated THz power and helps in detecting the received T-wave with a lock-in amplifier. The T-wave is transmitted via a silicon lens and redirected to the lensed Rx antenna by an off-axis parabolic mirror.

For characterizing the PIPED Tx performance, we determine the emitted power as a function of frequency by comparison to a commercially available THz reference Tx (Toptica, EK - 000724), see Methods. To ensure traceability, the emitted power  $P_{\text{THz,ref}}$  of the reference Tx was measured by using a calibrated pyroelectric thin-film sensor. We then detect the emission of the PIPED and the reference Tx by a commercially available photoconductive THz receiver (Toptica, EK 000725). The THz power  $P_{\text{THz,PIPED}}$  generated by the PIPED Tx leads to

a current  $I_{\text{Rx,PIPED}}$  in the reference receiver, while the emission of the reference Tx generates a receiver current  $I_{\text{Rx,ref}}$ . The PIPED THz output power can then be estimated by

$$P_{\text{THz,PIPED}} = P_{\text{THz,ref}} \left( I_{\text{Rx,PIPED}} / I_{\text{Rx,ref}} \right)^2. \quad (13)$$

The frequency dependence of the THz power emitted by the PIPED is shown in Fig. 3b. The PIPED is capable of generating radiation at frequencies of up to 1 THz. The measured transmitted power  $P_{\text{THz,PIPED}}$  obtained according to Eq. (13) is depicted as a blue solid line. For comparison, we perform a simulation of the THz power that the PIPED emits into free space via the silicon substrate and an adjacent silicon lens – the results are plotted as a solid red line. Details of the simulation can be found in the Methods and in Supplementary Section 9. The shapes of the measured and the simulated frequency characteristics coincide reasonably well, but the absolute power levels obtained from the measurement are approximately 14 dB below the simulated values. We attribute this effect to losses in the setup and to imperfect coupling of the PIPED THz beam to the reference Rx. The peaks in the simulated and the measured frequency characteristic are caused by antenna and bias line resonances. The roll-off at larger frequencies is predominantly caused by the carrier transit time in the 100 nm-wide silicon core of the PIPED, see Supplementary Section 9. This width can be further reduced<sup>28</sup> to, e. g., 75 nm, which would decrease the transit time accordingly. To avoid irreversible damage of the device in our Tx experiments, we chose to limit the optical power such that the mean photocurrent does not exceed 50  $\mu\text{A}$ . The measured radiated output power exhibits a maximum of approximately –55 dBm at 0.3 THz. Note that this value as well as its simulated counterpart of approximately –40 dBm are still well below the power levels that can be achieved by state-of-the art discrete THz sources. As an example, commercially available electronic multipliers (www.vadiodes.com) permit output powers of tens of milliwatts at 0.3 THz when operated with input powers of hundreds of milliwatts at 150 GHz, and similar power levels can be achieved with IMPATT diodes (www.terasense.com). However, these devices are limited to certain frequency bands or even to single-frequency operation for the case of IMPATT diodes. Photomixing in high-speed UTC-PD on III - V-substrates allows for broadband operation, with power levels of up to 1.2 mW at 0.3 THz achieved for a pair of devices operated in parallel<sup>21</sup>. The power level of our commercial THz reference Tx amounts to –19 dBm at 0.3 THz, measured by a calibrated photodetector, see Supplementary Section 2. In comparison to these established THz generators, our current PIPED devices are still inferior in terms of maximum output power. Note, however, that the PIPED approach exploits the intrinsic scalability advantages of highly mature silicon photonic integration and is hence perfectly suited for integrated T-wave signal processing systems that combine

the T-wave Tx and Rx on a common chip. These systems can be operated at very low powers levels as shown in the next section. In addition, the output power of PIPED systems can be further increased. For instance, the maximum applied current of 50  $\mu\text{A}$  is still well below the actual damage threshold of the PIPED – we expect that much higher operation currents can be safely applied provided that the devices are thermally connected to a proper heat sink, see Supplementary Section 5. Moreover, the output power can be increased by connecting an array of devices to a single antenna or transmission line, see Supplementary Section 12. Exploiting the coherent superposition of the individual THz currents, an array of  $n$  synchronously pumped PIPED connected in parallel would increase the THz output power of the Tx by a factor of  $n^2$ . The small PIPED length of roughly 1  $\mu\text{m}$ , the small capacitance below 1 fF, and the large resistance in excess of 10 k $\Omega$  would easily allow to connect  $n = 10$  PIPED to the antenna feed point, leading to a power gain of 20 dB. Moreover, the intrinsic scalability of silicon photonics allows building large-scale antenna arrays on a single chip, which could further increase the output power as well as the directivity of the emitted THz power.

For evaluating the PIPED Rx performance, we use a commercially available Tx (Toptica, EK - 000724). According to Eq. (12), the baseband photocurrent amplitude  $\hat{I}_{\text{BB},1}$  depends linearly on the amplitude  $\hat{U}_{\text{Rx},1}$  of the THz voltage, which is proportional to the square root of the THz power  $P_{\text{THz}}$ . As a metric for the Rx sensitivity, we can hence define the ratio

$$\Gamma = \frac{\hat{I}_{\text{BB},1}}{\sqrt{P_{\text{THz}}}} \propto \left. \frac{dS_{\text{Rx}}}{dU_{\text{Rx}}} \right|_{U_{\text{Rx},0}} \hat{P}_{\text{Rx},1}, \quad (14)$$

which describes the conversion factor from THz signal to baseband photocurrent. The linear relationship between  $\hat{I}_{\text{BB},1}$  and  $\sqrt{P_{\text{THz}}}$  is experimentally confirmed, see Supplementary Section 4. The conversion factor depends on the sensitivity slope  $dS_{\text{Rx}}/dU_{\text{Rx}}|_{U_{\text{Rx},0}}$ , see Eq. (12). This is experimentally confirmed by measuring the conversion factor  $\Gamma$  in dependence of the bias voltage  $U_{\text{Rx},0}$  at a frequency of 0.3 THz. The result is depicted in Fig. 3c (green, left axis) along with the slope of the sensitivity (blue, right axis) derived from the static  $S(U)$  characteristic in Fig. 2c. The two curves are in fair agreement. We further verify that the conversion factor depends linearly on the incident optical power  $\hat{P}_{\text{Rx},1}$ , see Supplementary Section 4. These findings confirm the validity of our PIPED model used to describe the Rx.

Similarly, we demonstrate the ability of a PIPED to perform broadband T/E conversion at the Rx. To this end, we measure the conversion factor  $\Gamma$  as a function of the THz frequency for two cases. In a first measurement, we leave the bias contacts open, which is denoted as switch position 0 in Fig. 3a (“zero bias-current operation”). This leads to the build-up of an internal

forward-bias of  $U_{\text{Rx},0} \approx 0.2 \text{ V}$  when illuminating the PIPED, see Supplementary Section 6. For the second measurement, we turn the switch in Fig. 3a to position 1 and connect an external DC voltage source  $U_{\text{Rx},0} = 0.45 \text{ V}$ . The results of the measured conversion efficiencies  $\Gamma$  are shown in Fig. 3d. The PIPED is able to receive radiation at frequencies up to 1 THz and beyond. At a frequency of 0.3 THz, the devices exhibit a conversion factor of  $95 \mu\text{A}/\sqrt{\text{W}}$  for bias voltages of  $U_{\text{Rx},0} = 0.45 \text{ V}$  and of  $44 \mu\text{A}/\sqrt{\text{W}}$  for zero bias current, i.e., internal bias voltages of  $U_{\text{Rx},0} \approx 0.2 \text{ V}$ . As expected from Fig. 3c, the bias voltage of 0.45 V leads to a larger slope  $dS_{\text{Rx}}/dU_{\text{Rx}}|_{U_{\text{Rx},0}}$  of the sensitivity and hence to a higher conversion factor as compared to the 0.2 V bias. The resonances in Fig. 3d and the drop of the conversion factor for larger frequencies are caused by the frequency response of the antenna, the PIPED and the bias lines.

If we assume a 50  $\Omega$  load, the conversion factor  $\Gamma$  can be translated to a conversion gain of  $\frac{1}{2}\Gamma^2 \times 50 \Omega$ , which corresponds to  $-73 \text{ dB}$  for zero bias-current operation and to  $-66 \text{ dB}$  for a bias voltage of 0.45 V. This is clearly below the conversion gain of  $-8.5 \text{ dB}$  that can be achieved by state-of-the-art electronic subharmonic mixers ([www.vadiodes.com](http://www.vadiodes.com)) operating at 300 GHz with a 150 GHz electronic local oscillator. Note, however, that the PIPED T-wave receivers can be tuned across a large range of operation frequencies that exceeds that of discrete SHM, which are usually limited to the specific transmission band of the waveguides needed to package the discrete devices and to block unwanted frequency components. Regarding optoelectronic down-conversion of T-waves signals, InP-based UTC-PD have been exploited<sup>42,44,45</sup>, leading to a conversion gain of  $-30 \text{ dB}$  at a frequency of 0.3 THz (ref. 42). However, down-conversion in UTC-PD relies on to the dynamic capacitance associated with accumulation of carriers in the absorption region and is hence only efficient for very high optical powers of, e.g., 80 mW (ref. 42). This leads to large DC currents and hence a strong noise background in the baseband current of, e.g.,  $28 \text{ nA}/\sqrt{\text{Hz}}$ , see Methods for details. Hence, despite the large conversion gain, the baseband signal-to-noise power ratio (SNR) of UTC-PD T-wave receivers is limited, and 57 dB  $\text{Hz}^{-1}$  have been demonstrated at a frequency of 0.3 THz for the devices of ref. 45. In contrast to that, PIPED exploit an intrinsically voltage-dependent sensitivity, Fig. 2c, and thus require only relatively small optical power levels. For a PIPED operated with zero bias current, we measure a noise current of  $9 \text{ pA}/\sqrt{\text{Hz}}$  and a SNR of 85 dB  $\text{Hz}^{-1}$  at 0.3 THz. These figures compare very well to the noise current of  $15 \text{ pA}/\sqrt{\text{Hz}}$  and the SNR of 91 dB  $\text{Hz}^{-1}$  reported for state-of-the-art photoconductors<sup>13</sup> as well as to the  $18 \text{ pA}/\sqrt{\text{Hz}}$  and 84 dB  $\text{Hz}^{-1}$  which we measured when replacing the PIPED Rx with the photoconductive reference Rx. The conversion gain of the reference Rx amounts to  $-67 \text{ dB}$  at 0.3 THz, see Supplementary Figure S1b, and is hence comparable to that of the PIPED Rx.

Based on these findings, we conclude that PIPED T-wave Rx can already now provide conversion factors and SNR levels that are comparable to those obtained by conventional III-V devices while offering ultra-compact footprint. It is also worth noting that the PIPED reported here are first-generation devices that still feature large potential for further performance improvements. As an example, using parallel arrays of  $n$  PIPED connected to a single Rx antenna would allow boosting the power conversion factor in proportion to  $n^2$ , hence allowing improvements of the conversion gain by one to two orders of magnitude, see Supplementary Section 12. Note also that the load resistance of  $50 \Omega$  assumed for translating the conversion factor  $\Gamma$  into a conversion gain is not the optimum choice: The PIPED itself features a large output impedance well above  $10 \text{ k}\Omega$ , and the conversion gain would hence increase if load resistances larger than  $50 \Omega$  could be used. Given the ultra-small capacitance of the PIPED, Supplementary Section 9, this would be possible without imposing significant RC limitations to the bandwidth of the device. These aspects indicate that PIPED-based T-wave Rx has the clear potential to unlock a wide variety of applications that rely on optoelectronic T-wave signal processing in compact integrated systems.

The SNR achieved with our PIPED Rx is sufficient for many spectroscopic or diagnostic applications, where lock-in detection and large integration times lead to a small detection bandwidth. Application of Rx-PIPED in high-speed THz communication would still require higher SNR, dictated by the large bandwidth of the data signal. Assuming that a viable transmission link requires a signal power that is at least 10 dB larger than the noise power in a 10 GHz signal bandwidth, the SNR needs to be larger than  $110 \text{ dB Hz}^{-1}$ . By using a high-power transmitter, e. g., an UTC-PD<sup>21</sup> or by using a T-wave amplifier<sup>38</sup>, T-wave powers of more than 0 dBm can be achieved, which would increase the SNR to more than  $100 \text{ dB Hz}^{-1}$ . Combining these transmitters with parallel arrays of PIPED that are connected to the same Rx antenna would lead to SNR values that are suitable for wireless communication links.

### Monolithically integrated T-wave system

To demonstrate the technological advantages of the PIPED concept, we monolithically integrate arrays of PIPED Tx and PIPED Rx on a common silicon chip. Tx and Rx are coupled by short T-wave transmission lines having various lengths  $L$  between  $10 \mu\text{m}$  and approximately 1 mm. An SEM picture of such a Tx-Rx pair is displayed in Fig. 4a. A  $1 \mu\text{m}$ -wide gap in the middle of the T-wave transmission line acts as a DC block to decouple the bias voltages of the Tx and the Rx. The insets show magnified pictures of the Tx, the Rx and the gap. In the experiment, we use the PIPED Tx and Rx to measure the amplitude and phase transfer characteristics of the transmission line at THz frequencies. Optical signals are fed to the Tx and the Rx PIPED by

separate silicon photonic waveguides equipped with grating couplers. The setup for measuring the transmission line characteristics is shown in Fig. 4b. As in the previous experiments, the Tx and Rx are fed with two optical spectral lines  $f_a$  and  $f_b$  at varying frequency separations. The Tx is biased in forward direction  $U_{\text{Tx},0} > 0$  and feeds the T-wave transmission line. At the end of the transmission line, the Rx PIPED acts as a homodyne receiver to coherently detect the T-wave signal and down-converts it to a baseband current  $I_{\text{BB},1}$ , see Eqs. (11) and (12). The Rx PIPED is operated under zero bias-current condition to minimize noise. Because the PIPED features a large impedance at THz frequencies, all transmission lines are essentially terminated by open circuits at both ends and thus act as T-wave resonators, for which the resonance frequencies are dictated by the respective geometrical length  $L$ . At the Rx, we measure the baseband photocurrent  $I_{\text{BB},1}$ . By sweeping the Tx frequency, we can separate the amplitude  $\hat{I}_{\text{BB},1}$  from the phase  $\varphi_{\text{BB}}$ , see Methods for details. To quantify the transmission line transfer characteristics, we use the complex transfer impedance  $\underline{Z}_{21} = |\underline{Z}_{21}| e^{j\varphi_{21}}$ , which is defined as the ratio of the complex T-wave voltage amplitude at the Rx PIPED and the complex T-wave current amplitude at the Tx PIPED. The magnitude of the complex transfer impedance is directly proportional to the baseband current amplitude  $\hat{I}_{\text{BB},1}$ ,

$$|\underline{Z}_{21}| = a \hat{I}_{\text{BB},1}, \quad (15)$$

where the proportionality factor  $a$  depends on the operation conditions of the Tx and the Rx PIPED,

$$a = \left( \frac{1}{2} \frac{dS_{\text{Rx}}}{dU_{\text{Rx}}} \Big|_{U_{\text{Rx},0}} \hat{P}_{\text{Rx},1} S_{\text{Tx}}(U_{\text{Tx},0}) \hat{P}_{\text{Tx},1} \right)^{-1}, \quad (16)$$

see Supplementary Section 7. The corresponding phase  $\varphi_{21}$  is obtained from  $\varphi_{\text{BB}}$  by swapping the role of the Tx and the Rx PIPED, thus allowing to eliminate the influence of the unknown group delay in the optical fibres, see Methods. The measured magnitude and phase characteristics of the transfer impedance  $\underline{Z}_{21,\text{meas}}$  are depicted as blue traces in Fig. 4c - e. For comparison, we have also numerically calculated the transfer impedance of the T-wave transmission lines using a commercially available time-domain solver. The results of the simulated transfer impedance  $\underline{Z}_{21,\text{sim}}$  are indicated as red traces in Fig. 4c - e. Note that calculating the proportionality factor  $a$  according to Eq. (16) is subject to large uncertainties since the experimental operating conditions of the Tx and Rx PIPED at THz frequencies are only approximately known. For estimating  $|\underline{Z}_{21}|$  from the measured baseband photocurrent amplitude  $\hat{I}_{\text{BB},1}$ , we have therefore chosen  $a$  such that we obtain best agreement of simulation and measurement, see Section 8 of the Supplementary Information. Moreover, we numerically correct for the frequency roll-off of the PIPED when deriving the measured transfer impedance  $\underline{Z}_{21,\text{meas}}$  from the baseband photocurrent amplitude  $\hat{I}_{\text{BB},1}$ . To

this end, the transit-time limited frequency response of both PIPED was approximated by an RC low-pass characteristic with a corner frequency of 0.3 THz, obtained from a least-squares fit of the measurement data, see Supplementary Section 8. The measured and the simulated transmission line characteristics show perfect agreement with respect to amplitude and phase over the entire frequency range  $f_{\text{THz}} = (0.05 \dots 0.8) \text{ THz}$ , corresponding to a span of 1.5 decades. The field distributions along the transmission lines have been investigated by numerical simulations of the structures, see Supplementary Section 10. These findings show that signal processing in PIPED can be quantitatively described by a reliable mathematical model, thus enabling deterministic photonic-electronic signal processing over an ultra-broadband frequency range.

### Summary and outlook

In summary, we have demonstrated a novel approach to T-wave signal processing that exploits internal photoemission at metal-semiconductor interfaces of silicon-plasmonic structures.

We show that T-wave transmitters and receivers can be monolithically co-integrated on the silicon photonic platform, thus enabling a novel class of photonic-electronic signal processors that may exploit the outstanding technical maturity and performance of the silicon photonic device portfolio. When used as a T-wave Rx, the performance of our current PIPED devices can already now compete with state-of-the-art III-V photoconductors, while further improvements are still possible by optimized device geometry and materials. The devices are analysed and described by a quantitatively reliable mathematical model. In a proof-of-concept experiment, we use co-integrated PIPED transmitters and receivers for measuring the complex transfer function of an integrated T-wave transmission line.

### References

- Nagatsuma, T., Ducournau, G. & Renaud, C. C. Advances in terahertz communications accelerated by photonics. *Nat. Photon.* **10**, 371–379 (2016).
- Koenig, S. *et al.* Wireless sub-THz communication system with high data rate. *Nat. Photon.* **7**, 977–981 (2013).
- Ma, J., Karl, N. J., Bretin, S., Ducournau, G. & Mittleman, D. M. Frequency-division multiplexer and demultiplexer for terahertz wireless links. *Nat. Commun.* **8**, 729 (2017).
- Capmany, J. & Novak, D. Microwave photonics combines two worlds. *Nat. Photon.* **1**, 319–330 (2007).
- Krügener, K. *et al.* Terahertz meets sculptural and architectural art: Evaluation and conservation of stone objects with T-ray technology. *Sci. Rep.* **5**, 14842 (2015).
- Shalit, A., Ahmed, S., Savolainen, J. & Hamm, P. Terahertz echoes reveal the inhomogeneity of aqueous salt solutions. *Nat. Chem.* **9**, 273–278 (2016).
- Tonouchi, M. Cutting-edge terahertz technology. *Nat. Photon.* **1**, 97–105 (2007).
- Fan, S., He, Y., Ung, B. S. & Pickwell-MacPherson, E. The growth of biomedical terahertz research. *J. Phys. D: Appl. Phys.* **47**, 374009 (2014).
- Stantchev, R. I. *et al.* Noninvasive, near-field terahertz imaging of hidden objects using a single-pixel detector. *Sci. Adv.* **2**, e1600190 (2016).
- Naftaly, M., Clarke, R. G., Humphreys, D. A. & Ridler, N. M. Metrology state-of-the-art and challenges in broadband phase-sensitive terahertz measurements. *Proc. IEEE* **105**, 1151–1165 (2017).
- Brown, E. R., McIntosh, K. A., Nichols, K. B. & Dennis, C. L. Photomixing up to 3.8 THz in low-temperature-grown GaAs. *Appl. Phys. Lett.* **66**, 285–287 (1995).
- Preu, S., Döhler, G. H., Malzer, S., Wang, L. J. & Gossard, A. C. Tunable, continuous-wave Terahertz photomixer sources and applications. *J. Appl. Phys.* **109**, 061301 (2011).
- Göbel, T. *et al.* Telecom technology based continuous wave terahertz photomixing system with 105 decibel signal-to-noise ratio and 3.5 terahertz bandwidth. *Opt. Lett.* **38**, 4197–4199 (2013).
- Sartorius, B., Stanze, D., Göbel, T., Schmidt, D. & Schell, M. Continuous wave terahertz systems based on 1.5  $\mu\text{m}$  telecom technologies. *J. Infrared Millim. Terahertz Waves* **33**, 405–417 (2011).
- Yu, X. *et al.* 160 Gbit/s photonics wireless transmission in the 300–500 GHz band. *APL Photonics* **1**, 081301 (2016).
- Puerta, R. *et al.* Single-carrier dual-polarization 328-Gb/s wireless transmission in a D-Band millimeter wave 2x2 MU-MIMO radio-over-fiber system. *J. Lightwave Technol.* **36**, 587–593 (2018).
- Hsieh, Y.-D. *et al.* Terahertz frequency-domain spectroscopy of low-pressure acetonitrile gas by a photomixing terahertz synthesizer referenced to dual optical frequency combs. *J. Infrared Millim. Terahertz Waves* **37**, 903–915 (2016).
- Hisatake, S., Koda, Y., Nakamura, R., Hamada, N. & Nagatsuma, T. Terahertz balanced self-heterodyne spectrometer with SNR-limited phase-measurement sensitivity. *Opt. Express* **23**, 26689–26695 (2015).
- Harter, T. *et al.* Wireless multi-subcarrier THz communications using mixing in a photoconductor for coherent reception. in *2017 IEEE Photonics Conference (IPC)* 147–148 (IEEE, 2017).
- Ishibashi, T., Muramoto, Y., Yoshimatsu, T. & Ito, H. Unitraveling-carrier photodiodes for terahertz applications. *IEEE J. Sel. Top. Quantum Electron.* **20**, 79–88 (2014).
- Song, H.-J. *et al.* Uni-travelling-carrier photodiode module generating 300 GHz power greater than 1 mW. *IEEE Microw. Wirel. Compon. Lett.* **22**, 363–365 (2012).
- Beling, A., Xie, X. & Campbell, J. C. High-power, high-linearity photodiodes. *Optica* **3**, 328–338 (2016).
- Berry, C. W. *et al.* High power terahertz generation using 1550 nm plasmonic photomixers. *Appl. Phys. Lett.* **105**, 011121 (2014).
- Olvera, A. D. J. F., Lu, H., Gossard, A. C. & Preu, S. Continuous-wave 1550 nm operated terahertz system using ErAs:In(Al)GaAs photo-conductors with 52 dB dynamic range at 1 THz. *Opt. Express* **25**, 29492–29500 (2017).
- Thomson, D. *et al.* Roadmap on silicon photonics. *J. Opt.* **18**, 073003 (2016).
- Vivien, L. & Pavesi, L. eds *Handbook of silicon photonics*. (Taylor & Francis, 2013).
- Bogaerts, W. *et al.* Nanophotonic waveguides in silicon-on-insulator fabricated with CMOS technology. *J. Lightwave Technol.* **23**, 401–412 (2005).
- Muehlbrandt, S. *et al.* Silicon-plasmonic internal-photoemission detector for 40 Gbit/s data reception. *Optica* **3**, 741–747 (2016).
- Harter, T. *et al.* Silicon-plasmonic photomixer for generation and homodyne reception of continuous-wave THz radiation. in *Conference on Lasers and Electro-Optics SM4E.5* (OSA, 2016).
- Lindenmann, N. *et al.* Photonic wire bonding: a novel concept for chip-scale interconnects. *Opt. Express* **20**, 17667–17677 (2012).
- Pfeifle, J., Alloati, L., Freude, W., Leuthold, J. & Koos, C. Silicon-organic hybrid phase shifter based on a slot waveguide with a liquid-crystal cladding. *Opt. Express* **20**, 15359–15376 (2012).
- Harris, N. C. *et al.* Efficient, compact and low loss thermo-optic phase shifter in silicon. *Opt. Express* **22**, 10487–10493 (2014).
- Kim, J.-Y. *et al.* Compact and stable THz vector spectroscopy using silicon photonics technology. *Opt. Express* **22**, 7178–7185 (2014).
- Reed, G. T., Mashanovich, G., Gardes, F. Y. & Thomson, D. J. Silicon optical modulators. *Nat. Photon.* **4**, 518–526 (2010).

35. Koos, C. *et al.* Silicon-organic hybrid (SOH) and plasmonic-organic hybrid (POH) integration. *J. Lightwave Technol.* **34**, 256–268 (2016).
36. Hiraki, T. *et al.* Heterogeneously integrated III–V/Si MOS capacitor Mach–Zehnder modulator. *Nat. Photon.* **11**, 482–485 (2017).
37. Timurdogan, E. *et al.* An ultralow power athermal silicon modulator. *Nat. Commun.* **5**, 4008 (2014).
38. Quay, R. *et al.* High-power microwave GaN/AlGaIn HEMTs and MMICs on SiC and silicon substrates for modern radio communication. *Phys. status solidi* **215**, 1700655 (2018).
39. Naik, G. V., Shalaev, V. M. & Boltasseva, A. Alternative plasmonic materials: Beyond gold and silver. *Adv. Mater.* **25**, 3264–3294 (2013).
40. Canali, C., Majni, G., Minder, R. & Ottaviani, G. Electron and hole drift velocity measurements in silicon and their empirical relation to electric field and temperature. *IEEE Trans. Electron Devices* **22**, 1045–1047 (1975).
41. Bowers, J. & Burrus, C. Ultrawide-band long-wavelength p-i-n photodetectors. *J. Lightwave Technol.* **5**, 1339–1350 (1987).
42. Renaud, C. C. *et al.* Antenna integrated THz uni-traveling carrier photodiodes. *IEEE J. Sel. Top. Quantum Electron.* **24**, 8500111 (2018).
43. Latzel, P. *et al.* Generation of mW Level in the 300-GHz band using resonant-cavity-enhanced untraveling carrier photodiodes. *IEEE Trans. Terahertz Sci. Technol.* **7**, 800–807 (2017).
44. Rouvalis, E., Fice, M. J., Renaud, C. C. & Seeds, A. J. Millimeter-wave optoelectronic mixers based on uni-traveling carrier photodiodes. *IEEE Trans. Microw. Theory Tech.* **60**, 686–691 (2012).
45. Hisatake, S., Kim, J.-Y., Ajito, K. & Nagatsuma, T. Self-heterodyne spectrometer using uni-traveling-carrier photodiodes for terahertz-wave generators and optoelectronic mixers. *J. Lightwave Technol.* **32**, 3683–3689 (2014).

## Acknowledgements

This work was supported by the European Research Council (ERC Starting Grant ‘EnTeraPIC’, # 280145; ERC Consolidator Grant ‘TeraSHAPE’, # 773248), by the Alfried Krupp von Bohlen und Halbach Foundation, by the Helmholtz International Research School of Teratronics (HIRST), by the Karlsruhe School of Optics and Photonics (KSOP), by Karlsruhe Nano Micro Facility (KNMF).

## Author contributions

T.H., S.M., W.F. and C.K. developed the idea. T.H., S.M., S.U. and L.H. contributed to the fabrication of the devices. T.H., S.M., W.F. and C.K. developed the mathematical formulation. T.H., S.M. and A.S. conducted the measurements. T.H. and S.N. performed experiments to calibrate the reference Tx and Rx. T.H. performed electromagnetic simulations. W.F. and C.K. supervised the project. T.H., W.F. and C.K. wrote the paper. All authors revised the paper.

## Conflict of interest

The authors declare no conflict of interest.

## Additional information

**Correspondence and requests for materials** should be addressed to T.H. or C.K.

## Methods

**Advantages of continuous-wave signal processing in highly integrated optoelectronic T-wave systems.** Optoelectronic generation and detection of T-wave signals can generally rely on photomixing of CW carriers or on direct detection of ultra-short laser pulses<sup>46,47</sup>. The focus of our work is on ultra-compact highly scalable T-wave generators and detectors that are amenable to dense integration on highly scalable photonic integration platforms. For such devices, CW operation is advantageous since it allows driving the PIPED from readily available CW laser sources that have been developed in the context of

optical communications, and that offer small footprints along with narrow optical linewidth and broadband wavelength tunability<sup>48,49</sup>. In contrast to that, chip-scale integration of pulsed laser sources is much more difficult, in particular when ultra-short pulses with durations of well below 1 ps are required. Moreover, when coupled to high index-contrast semiconductor-based waveguides with small cross section, pulsed optical signals with low duty cycles are often subject to nonlinear absorption, e.g., caused by two-photon processes and the resulting free carriers<sup>50</sup>.

**PIPED device fabrication.** The PIPED are fabricated on commercially available silicon-on-insulator (SOI) substrates with a 340 nm thick device layer. The waveguide structures are defined by electron beam lithography and reactive ion etching. Directional metal evaporation under various angles allows to deposit different metals on each side of the silicon core and enables the fabrication of an asymmetrically metallized silicon core which has a width as small as 100 nm and below<sup>28</sup>. To keep the fabrication simple, we use gold (Au) and titanium (Ti) to metallize the silicon core sidewalls since these materials were readily available in our laboratory. Note that other metals such as copper or aluminium with similar optical and electrical properties could be used as well, thus allowing PIPED fabrication using standard CMOS materials. During metallization, an undercut hard mask on top of the silicon core is used to prevent a short circuit between the Au and the Ti region, see Fig. 2a. For more information on the fabrication of the PIPED see ref. 28.

**Coherent T-wave detection.** For sensitive detection of the Rx current  $\hat{I}_{BB,1}(t)\cos(\varphi_{BB})$ , a lock-in amplifier is used. To this end, we modulate the Tx bias voltage  $U_{Tx,0}$ , which leads to a modulation of the THz Tx current  $\hat{I}_{Tx,1}(t)$ , of the received THz voltage  $\hat{U}_{Rx,1}(t)$ , and of the time-variant part  $\hat{I}_{BB,1}$  of the baseband photocurrent, see Eq. (12). The modulation frequency is set to  $f_{LI} = 12.2$  kHz, and the modulated receiver current  $\hat{I}_{BB,1}(t)\cos(\varphi_{BB})$  is measured by a lock-in amplifier (Toptica TeraControl 110). The phase  $\varphi_{BB}$  of the baseband current depends on the phase  $\varphi_{Tx,THz}$  of the optical power beat at the Tx, the phase  $\varphi_{Rx,THz}$  of the optical power beat at the Rx, as well as on the phase delay  $\varphi_{TxRx}$  gathered during transmission of the T-wave from the Tx to the Rx,

$$\varphi_{BB} = \varphi_{Tx,THz} - \varphi_{Rx,THz} + \varphi_{TxRx} \quad (17)$$

For homodyne detection, see Fig. 3a and Fig. 4b, the phase difference  $\varphi_{Tx,THz} - \varphi_{Rx,THz}$  of the optical power beats depends only on the optical group delay  $\tau_{opt}$  between the Tx and the Rx,

$$\varphi_{Tx,THz} - \varphi_{Rx,THz} = \omega_{THz} \tau_{opt} = 2\pi f_{THz} n_g \Delta L / c \quad (18)$$

where  $c$  is the speed of light,  $n_g$  the optical group refractive index of the single-mode fibres and  $\Delta L$  the path length difference of the optical wave. In this relation, we assumed that the on-chip SOI waveguide at the Tx and the Rx have the same length. Scanning the frequency  $f_{THz}$  leads to an oscillation of the current  $\hat{I}_{BB,1}\cos(\varphi_{BB})$ , where the number of oscillations per frequency interval depends on the time delay  $\tau_{opt}$ . We record the current  $\hat{I}_{BB,1}\cos(\varphi_{BB})$  as a function of the THz frequency  $f_{THz}$  and separate the amplitude  $\hat{I}_{BB,1}$  from the phase  $\varphi_{BB}$  by means of a Fourier transformation of the received signal  $\hat{I}_{BB,1}\cos(\varphi_{BB}) = \frac{1}{2} \hat{I}_{BB,1} [e^{j\varphi_{BB}} + e^{-j\varphi_{BB}}]$ . After Fourier transformation, we numerically remove the negative frequency components and calculate the inverse Fourier transform to obtain the complex amplitudes  $\frac{1}{2} \hat{I}_{BB,1} e^{j\varphi_{BB}}$  of the frequency-dependent baseband current. From these complex amplitudes, we can directly read the received current amplitude  $\hat{I}_{BB,1}$  and the phase  $\varphi_{BB}$ . Regarding the phase information, we are mainly interested in the phase delay  $\varphi_{TxRx}$  accumulated by the T-wave during propagation from the Tx to the Rx. To obtain this information, we need to eliminate the phase shifts that are caused by the unknown optical group delay  $\tau_{opt}$  between the Tx and the Rx. To this end, we perform two consecutive measurements and exploit the fact that the same PIPED can act both as Tx and as Rx. The first measurement is performed as described in Fig. 4b. In the second measurement we swap the role of Tx and Rx by switching the bias conditions of the associated PIPED. Since the optical beam path is unchanged, only the sign of  $\varphi_{Tx,THz} - \varphi_{Rx,THz}$  has changed, while  $\varphi_{TxRx}$  is unchanged. For Eq. (17), the THz phase can then be calculated,

$$\varphi_{TxRx} = (\varphi_{BB,norm} + \varphi_{BB,rev}) / 2 \quad (19)$$

The amplitude of the baseband current  $\hat{I}_{\text{BB},1,\text{rev}}$  is not changed by reversing Tx and Rx. In Fig. 4c-e the plotted baseband current  $\hat{I}_{\text{BB},1}$  was taken as the mean of both measurements

$$\hat{I}_{\text{BB},1} = (\hat{I}_{\text{BB},1,\text{norm}} + \hat{I}_{\text{BB},1,\text{rev}}) / 2 \quad (20)$$

**Calibration and traceability of THz power measurements:** All measurements of THz power levels rely on a commercially available reference Tx (Toptica, EK 000724). To ensure traceability of our measurement results, we determine the power emission of the reference Tx by using a dedicated pyroelectric thin-film detector (Sensor- und Lasertechnik Dr. W Bohmeyer, THz20) that has been calibrated (73413-PTB-14) by the Physikalisch-Technische Bundesanstalt (PTB) Berlin (German National Metrology Institute). Note that this detector does not allow detecting THz powers below 1  $\mu\text{W}$  due to limited sensitivity. For detecting the sub-1  $\mu\text{W}$  emission powers of our PIPED Tx, we use a commercially available photoconductive Rx (Toptica, EK 000725) to determine the ratio of the PIPED emission power and the known emission power of the Toptica reference Tx, see Eq. (13) and the corresponding discussion.

**3D EM simulations.** The response of the THz dipole antenna, see Fig. 3b, and the THz resonators, see Fig. 4c-e, are simulated using a commercially available numerical time-domain solver (CST Microwave Studio, www.cst.com). A crucial aspect is the correct representation of the thin metal layers of the transmission lines and the antennae. Atomic force microscope measurements reveal a 110 nm-thick gold layer on top of a 40 nm-thick titanium layer. In the simulation of transmission lines with dimensions in the mm-range, a detailed representation of the field within the metal would lead to an unrealistic number of mesh cells that cannot be handled with the available computing resources. Therefore, we use the “thin panel” option of CST microwave studio, which relates the tangential electric and magnetic fields on the surface of the metal with the help of surface impedances. The Rx and the Tx PIPED are described by discrete equivalent circuits. For simulation of the Tx as depicted in Fig. 3b, the PIPED is represented by a current source in parallel to a capacitance. Details on the antenna simulation can be found in Supplementary Section 9. The antenna is simulated as a thin metal panel on a silicon substrate with open boundaries to emulate an infinite half-space below. This approach is valid because the silicon chip is in direct contact with a macroscopic silicon lens with dimensions much larger than the THz wavelength or the Tx antenna. The total radiated power corresponds to the total power radiated in the lower silicon half-space. For a numerical analysis of the THz resonator in Fig. 4, all transmission line structures are again represented as thin metal panels deposited on a semi-infinite silicon substrate. The Tx PIPED is modelled as a current source, and the Rx PIPED is modelled as an open circuit across which the voltage is measured. In both cases, we obtain essentially the same results when replacing the ideal current source or open circuit with infinite internal resistances by devices that feature finite internal resistances of 10 k $\Omega$ . This is a worst-case estimate of the real internal PIPED resistance which is typically well above the assumed value of 10 k $\Omega$ , see Supplementary Section 7. The complex transfer impedance can be calculated by dividing the simulated THz voltage amplitude at the Rx by the THz current amplitude at the Tx. Alternatively, the complex transfer impedance  $Z_{21}$  can be derived from numerically calculated S-parameters of the THz resonator, see Supplementary Section 11. Both methods lead to the same results.

**Optical setup.** For generating the optical power beat, two temperature-controlled tunable distributed feedback (DFB) lasers with linewidths of around 1 MHz are used (#LD-1550-0040-DFB-1). The difference frequency can be tuned from 0 to 1.2 THz with a relative frequency accuracy better than 10 MHz and an absolute frequency accuracy of 2 GHz. For feeding of light from single-mode fibres to antenna-coupled PIPED, Fig. 3a, we use grating couplers with losses of 5 dB, followed by 0.9 mm-long on-chip SOI waveguides with propagation losses of 2.3 dB/mm, thus leading to total coupling loss of 7 dB. For the integrated THz system, Fig. 4b, the grating coupler losses amount to 5.3 dB, the waveguide propagation losses to 1.1 dB/mm, and the length of the on-chip waveguide is 0.6 mm. This leads to total coupling losses of 6 dB. The optical path length difference  $\Delta L$  between the Tx and the Rx was between 1.0 m and

1.3 m for the antenna-coupled PIPED, Fig. 3a, and 0.6 m for the integrated THz system, Fig. 4. For the antenna-coupled PIPED, the T-wave Tx and the Rx characteristics were sampled with steps of 10 MHz, Fig. 3b,d, and the integration time of the lock-in amplifier was chosen between 20 ms and 100 ms. For spectral characterization of the integrated T-wave systems, Fig. 4c-e, sampling points were taken every 25 MHz, and the integration time was set to 100 ms.

**SNR measurements and benchmarking.** For characterizing the noise performance of our devices, we measure the short-circuit root-mean-square noise current  $\sqrt{\langle i_N^2 \rangle}$  within a known detection  $B$  for the case that there is no input T-wave signal<sup>51</sup>. To this end, we use a lock-in amplifier (Toptica TeraControl 110), which, according to the manufacturer, features an equivalent noise bandwidth of  $B = 1/(2T)$  for a given integration time  $T$ . For zero bias current, the device is driven by its internal bias voltage of 0.2 V only, and the noise current amounts to  $9 \text{ pA}/\sqrt{\text{Hz}}$ . For better comparability to widely used THz spectroscopy systems, we also determine the signal-to-noise power ratio (SNR) obtained in our experiment. Using the Toptica reference transmitter (EK-000724), the T-wave power incident on the Rx at 0.3 THz amounts to  $P_{\text{THz}} = -19 \text{ dBm}$  and leads to an SNR of 85 dB Hz<sup>-1</sup>. A similar SNR of 84 dB Hz<sup>-1</sup> is obtained by using the Toptica reference receiver. For the externally applied bias voltage  $U_{\text{Rx},0} = 0.45 \text{ V}$ , the RMS noise current increases considerably to values of  $190 \text{ pA}/\sqrt{\text{Hz}}$ , thus reducing the achieved SNR at 0.3 THz to 65 dB Hz<sup>-1</sup> despite the larger conversion factor. The strong noise level for the case of an externally applied bias voltage is attributed to the DC voltage source. Improved noise levels might be achieved by low-pass filtering the bias voltage.

In our manuscript, we give the SNR power ratio in units of dB Hz<sup>-1</sup>, which is independent of the integration time of the lock-in detection. Other groups<sup>13,45</sup> specify the SNR in dB in combination with the integration time  $T$  of the lock-in detector. To compare these values to our results, we convert the SNR of ref. 13 and ref. 45 to dB Hz<sup>-1</sup>. From Fig. 3 in ref. 13 we read an SNR of 93 dB at 0.3 THz. In this measurement, the lock-in filter slope was set to 12 dB/octave and an integration time of  $T = 200 \text{ ms}$  was used. This leads to an equivalent noise bandwidth of  $B = 1/(8T) = 0.625 \text{ Hz}$  (Research Stanford Systems SR844 user manual, www.thinksrs.com/downloads/pdfs/manuals/SR844m.pdf) and an SNR value of 91 dB Hz<sup>-1</sup> as stated in the main text. In ref. 45, the measured SNR value is 47 dB and an integration time of 23.4 ms was used. The filter slope is not explicitly stated. By assuming a filter slope of 6 dB/octave, we get an equivalent noise bandwidth of  $B = 1/(4T) = 10.7 \text{ Hz}$  and therefore an SNR of 57 dB Hz<sup>-1</sup>. The baseband noise background of  $28 \text{ nA}/\sqrt{\text{Hz}}$  mentioned on the main text for ref. 44 was estimated from the noise floor of  $-105 \text{ dBm Hz}^{-1}$  assuming a 50  $\Omega$  load.

**Data availability.** The data that support the plots within this paper and other findings of this study are available from the corresponding author upon reasonable request.

## References

46. Berry, C. W., Wang, N., Hashemi, M. R., Unlu, M. & Jarrahi, M. Significant performance enhancement in photoconductive terahertz optoelectronics by incorporating plasmonic contact electrodes. *Nat. Commun.* **4**, 1622 (2013).
47. Dietz, R. J. B. *et al.* Influence and adjustment of carrier lifetimes in InGaAs/InAlAs photoconductive pulsed terahertz detectors: 6 THz bandwidth and 90dB dynamic range. *Opt. Express* **22**, 19411–19422 (2014).
48. van Dijk, F. *et al.* Integrated InP heterodyne millimeter wave transmitter. *IEEE Photonics Technol. Lett.* **26**, 965–968 (2014).
49. Ponnampalam, L. *et al.* Monolithically Integrated Photonic Heterodyne System. *J. Lightwave Technol.* **29**, 2229–2234 (2011).
50. Vallaitis, T. *et al.* Optical properties of highly nonlinear silicon-organic hybrid (SOH) waveguide geometries. *Opt. Express* **17**, 17357–17368 (2009).
51. Roggenbuck, A. *et al.* Coherent broadband continuous-wave terahertz spectroscopy on solid-state samples. *New J. Phys.* **12**, 043017 (2010).

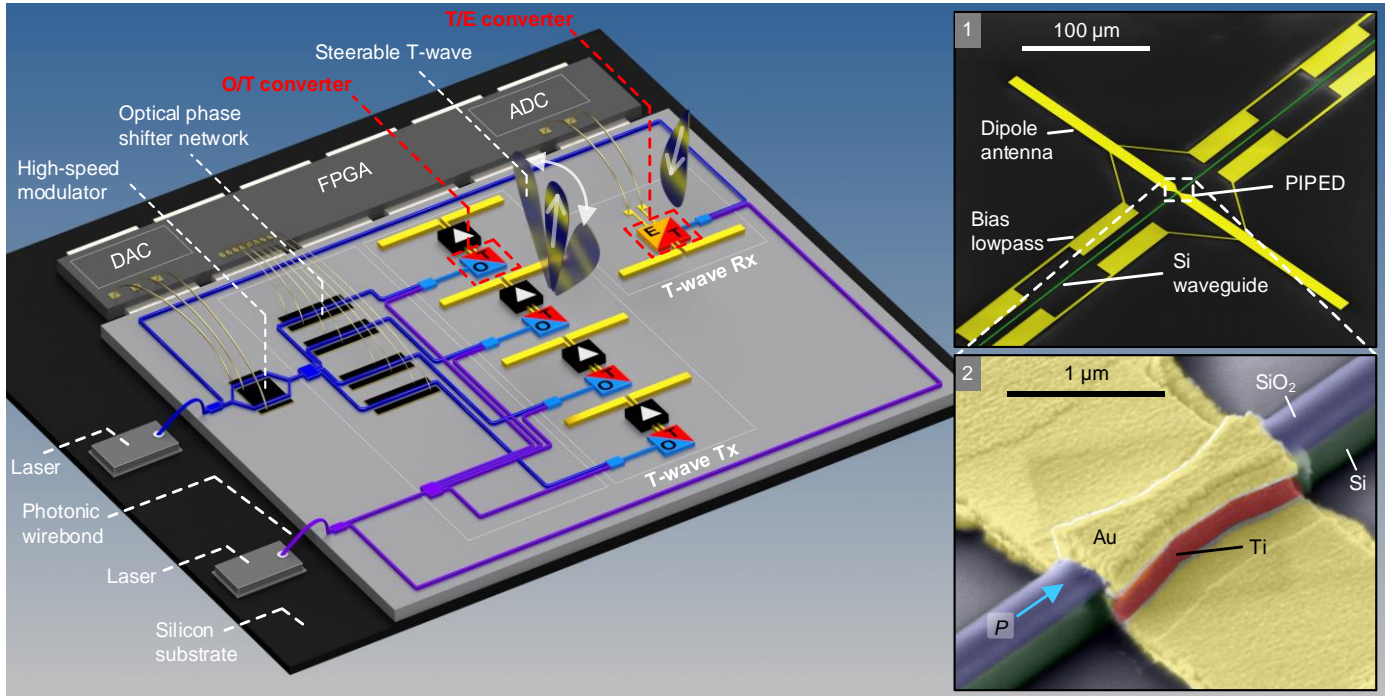


**Figure 1** Vision of an integrated silicon-plasmonic T-wave wireless transceiver that exploits optoelectronic signal processing both at the transmitter and at the receiver. The system combines optical-to-T-wave (O/T) and T-wave-to-electronic (T/E) converters with advanced silicon photonic devices such as phase shifters or high-performance modulators. Continuous-wave (CW) lasers are coupled to the chip using photonic wire bonds<sup>30</sup>, and electrical circuits such as field-programmable gate arrays (FPGA), digital-to-analogue and analogue-to-digital converters (DAC and ADC) are used to drive the modulators and to process the received signals. The transmitter comprises a T-wave antenna array, fed by an array of O/T converters that are driven by a series of optical signals. The phases of the optical and hence the T-wave signals can be precisely defined by an electrically driven optical phase shifter network, thereby enabling broadband beam steering. Optionally, additional T-wave amplifiers could boost the power of the generated signals. Coherent detection of the T-wave signal relies on a pair of optical carriers, the power beat of which serves as a local oscillator for T/E conversion. **Inset 1:** False-colour scanning electron microscopy (SEM) image of an O/T or T/E converter. The devices rely on plasmonic internal-photoemission detectors (PIPED<sup>28</sup>) that are coupled to dipole antennae. The PIPED are fed through silicon photonic waveguides and biased via low-pass structures that are directly connected to the arms of the antennae. **Inset 2:** Detailed view of a fabricated PIPED. The device consists of a narrow silicon nanowire waveguide that is combined with overlays of gold (Au) and titanium (Ti) to form an ultra-small plasmonic structure with two metal-semiconductor interfaces. The optical power  $P$  is fed to the PIPED with by a silicon photonic waveguide.

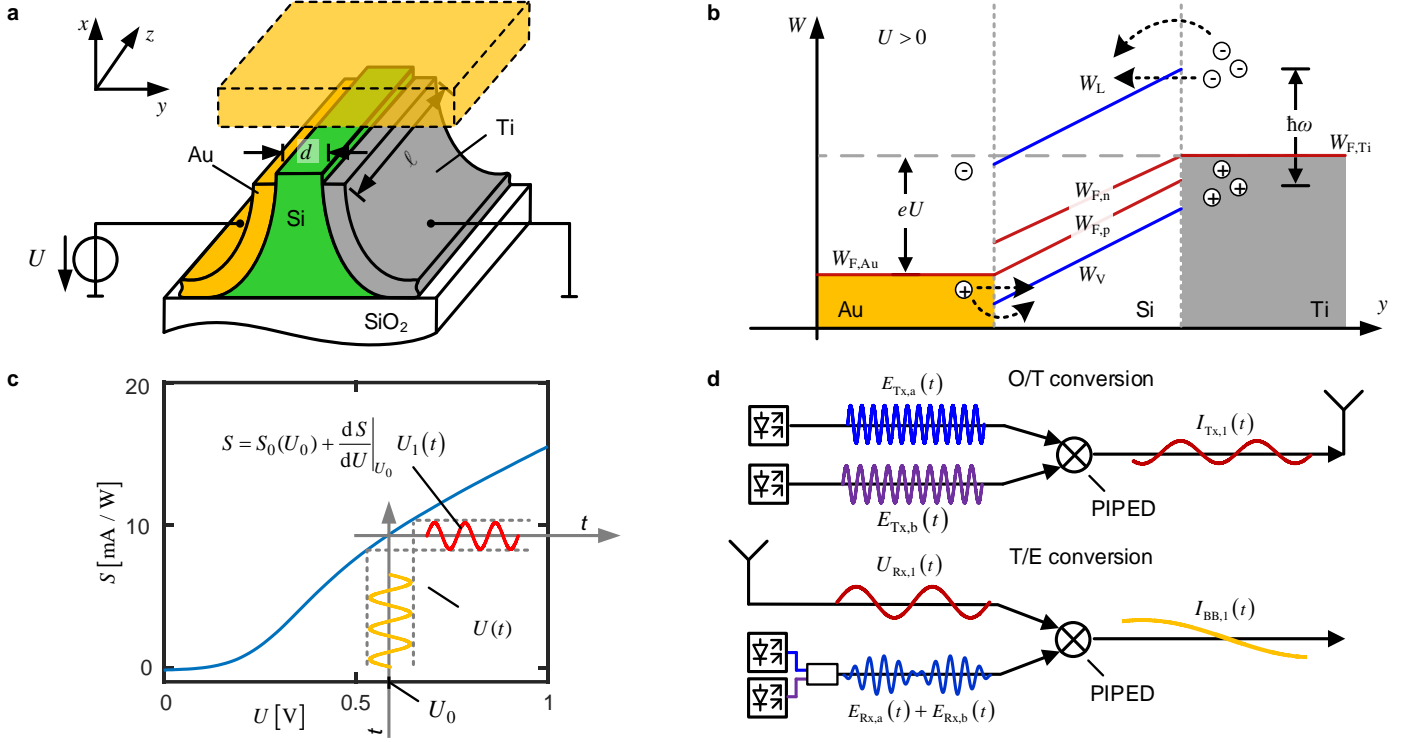


**Figure 2** Operating principle of PIPED-based T-wave transmitters and coherent receivers. **a**, Schematic of the PIPED, consisting of a silicon core with a gold and a titanium sidewall. Surface plasmon polaritons (SPP) propagating along the  $z$ -direction are mostly absorbed in the Ti due to the large imaginary part of its complex electric permittivity  $\epsilon_r$ . A voltage  $U$  is applied between the Au and the Ti electrode. **b**, Band diagram of the Au-Si-Ti junction. The quantities  $W_L$  and  $W_V$  denote the edge of the conduction and the valance band in the silicon core, and the Fermi levels in gold and titanium are denoted as  $W_{F,Au}$  and  $W_{F,Ti}$ , respectively. The applied voltage  $U > 0$  and the injection of carriers due to absorption of light lead to an interband non-equilibrium, which is described by the separation of the quasi-Fermi levels of conduction-band electrons and valence-band holes, denoted as  $W_{F,n}$  and  $W_{F,p}$ , respectively. Photons absorbed in the Ti layer excite hot electrons, which can overcome or tunnel through the Schottky potential barrier, leading to a photocurrent  $I = SP$ . An equivalent effect occurs for holes at the Au-Si-interface – the relative magnitude of the two contributions is still under investigation. The carrier emission probability into the Si waveguide core and therefore the sensitivity  $S(U)$  can be increased ( $U > 0$ ) or decreased ( $U < 0$ ) by varying the bias voltage  $U$ . **c**, Measured sensitivity  $S(U)$  of the PIPED in dependence of the applied voltage  $U$ . In the vicinity of a bias voltage  $U = U_0$ , the sensitivity  $S(U)$  can be linearized. **d**, In essence, the PIPED can be used as a mixer that multiplies two signals to generate a waveform at the difference-frequency. **Upper Subfigure**: When used for photomixing (O/T conversion) at the T-wave transmitter (Tx), the PIPED acts as a quadratic detector and the output photocurrent  $I_{Tx,i}(t)$  corresponds to the product of two time-dependent optical signals  $E_{Tx,a}(t)$  and  $E_{Tx,b}(t)$ . **Lower Subfigure**: When used for optoelectronic down-conversion (T/E conversion) at the T-wave receiver (Rx), the PIPED combines two functionalities, namely the generation of a THz local oscillator (LO) from two optical carriers  $E_{Rx,a}(t)$  and  $E_{Rx,b}(t)$  and the down-conversion of the received T-wave to the baseband. To this end, the PIPED is fed by a superposition of two unmodulated optical carriers, oscillating at frequencies  $f_{Rx,a}$  and  $f_{Rx,b}$ , while a time-dependent voltage  $U_{Rx,i}(t)$  modulates the device sensitivity. The PIPED photocurrent is then given by the product of the time-variant sensitivity with the time-variant optical power  $P_{Rx}(t)$ .

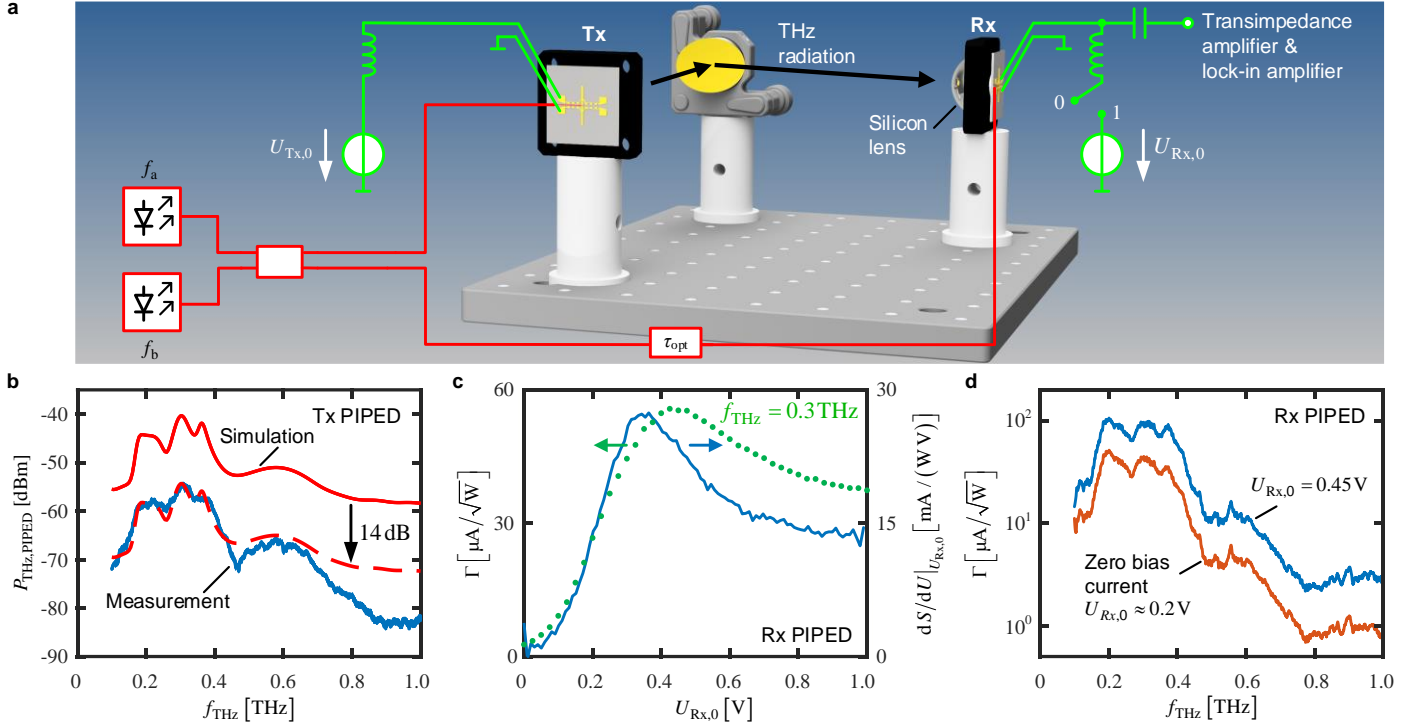


**Figure 3** Demonstration of PIPED performance for O/T and T/E conversion. **a**, Experimental setup. For measuring the PIPED Tx (Rx) separately, the respective other component is replaced by a commercially available device in a free-space setup. Light from two lasers with frequencies  $f_a$  and  $f_b$  is superimposed to generate an optical power beat at  $f_{\text{THz}} = |f_a - f_b|$ , which generates a T-wave in the PIPED Tx or acts as a local oscillator (LO) for homodyne detection in the PIPED Rx. When using the PIPED at the Tx, the device is biased by a DC voltage  $U_{\text{Tx},0}$ , which is modulated by an AC signal for lock-in detection. The bias is applied to the PIPED Tx via dedicated on-chip low-pass structures (“THz chokes”), see Inset 1 of Fig. 1. The same structures are used at the PIPED Rx, along with an additional bias-T in the feed circuit that allows separating the DC bias from the AC lock-in signal. The AC signal is fed to a transimpedance amplifier and detected by a lock-in amplifier. When operating the PIPED as a T-wave Rx, we either apply a defined bias voltage  $U_{\text{Rx},0}$  by connecting an external voltage source (switch position 1), or we leave the bias contacts open (switch position 0, “zero bias current”), which leads to a build-up of an internal forward-bias of  $U_{\text{Rx},0} \approx 0.2 \text{ V}$  upon illumination of the PIPED. **b**, PIPED as T-wave Tx. The radiated power (blue) was determined by a commercial reference Rx (Toptica, EK 000725). The Tx antenna and the THz chokes were designed for a resonance frequency of 0.385 THz, see Supplementary Section 3 for details. The peaks at lower frequencies are caused by unwanted resonances on the choke structures. For comparison, we also plot the simulated THz power (solid red) emitted by the PIPED via the silicon substrate and an adjacent silicon lens. The shape of the measured frequency characteristic coincides reasonably well with its simulated counterpart, while the absolute power levels obtained from the measurement are approximately 14dB below the simulated values. We attribute this to losses in the setup and to imperfect coupling of the PIPED THz beam to the reference Rx. For better comparison of the shapes, we shifted the simulated characteristic by 14 dB (dashed red) to coincide with the measurement. Details of the simulation can be found in the Methods and in Supplementary Section 9. **c**, PIPED as T-wave Rx. Measured conversion factor  $\Gamma = \hat{I}_{\text{BB},1} / \sqrt{P_{\text{THz}}}$  (green) as a function of Rx bias voltage  $U_{\text{Rx},0}$ . The bias-dependent sensitivity slope  $dS/dU|_{U_{\text{Rx},0}}$  (blue) features a maximum that deviates slightly from the maximum of the conversion factor  $\Gamma$  at a carrier frequency of 0.3THz. We attribute this effect to the voltage-dependence of the transit time. **d**, Conversion factor  $\Gamma$  of the Rx as a function of the THz frequency both for zero bias-current operation ( $U_{\text{Rx},0} \approx 0.2 \text{ V}$ ) and for an externally applied DC bias of  $U_{\text{Rx},0} = 0.45 \text{ V}$ , which leads to the maximum conversion factor, see Sub-figure (c).

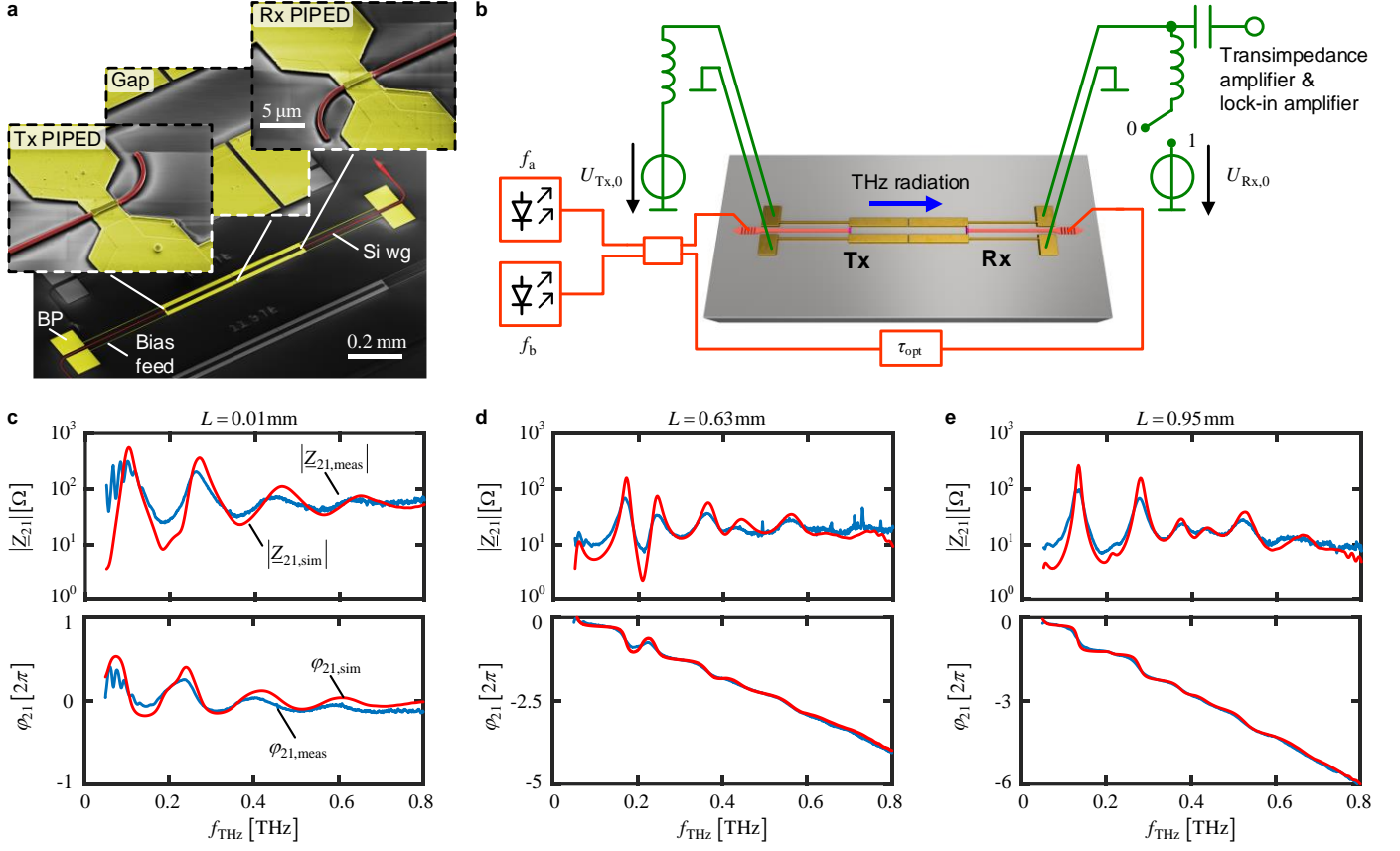


**Figure 4** Demonstration of T-wave system on a silicon chip. **a**, False-colour SEM image of the THz system, consisting of a T-wave Tx, a coplanar transmission line, and a T-wave Rx. Light is coupled to the PIPED Tx and Rx by silicon waveguides. Bias pads (BP) and THz-blocking bias feeds (“THz chokes”) allow to apply a voltage to, or to extract a signal current from the PIPED. A gap in the middle of the transmission line separates the bias voltages of Tx and the Rx. The insets show magnified SEM images of Tx, Rx and the transmission line gap. **b**, Experimental setup for the on-chip transmission line measurements. The Tx and Rx are fed with two optical spectral lines  $f_a$  and  $f_b$  at varying frequency separations. The Tx is biased in forward direction  $U_{Tx,0} > 0$  and feeds the T-wave transmission line. At the end of the transmission line, the Rx PIPED acts as a homodyne receiver to coherently detect the T-wave signal by down-conversion to the baseband current  $I_{BB,1}$ . To reduce the noise, the switch is set to 0 to operate the Rx PIPED with zero-bias current. **c - e**, Magnitude and phase characteristics of the complex transfer impedance  $Z_{21} = |Z_{21}| \exp(j\varphi_{21})$ . The red curves show the simulated frequency characteristics of  $|Z_{21,sim}|$  and  $\varphi_{21,sim}$  for three transmission line lengths  $L = (0.01, 0.63, 0.95)$  mm, and the blue curves represent the corresponding measurement results,  $|Z_{21,meas}|$  and  $\varphi_{21,meas}$ . The frequency roll-off of the PIPED is modelled by an RC-low pass with a 3dB-frequency of  $f_{3dB} = 0.3$  THz, see Supplementary Section 8. The measurements (blue) agree very well with the simulation (red).